



Preparation of a direct Z-scheme $\alpha\text{-Fe}_2\text{O}_3/\text{MIL}-101(\text{Cr})$ hybrid for degradation of carbamazepine under visible light irradiation

Quan Huo, Xiaoran Qi, Jianshu Li, Gongquan Liu, Yao Ning, Xubiao Zhang, Boyu Zhang, Yanfei Fu, Suyan Liu*

Hebei Key Laboratory of Applied Chemistry, School of Environmental and Chemical Engineering, Yanshan University, Qinhuangdao 066004, Hebei, People's Republic of China



ARTICLE INFO

Keywords:

$\alpha\text{-Fe}_2\text{O}_3$
MIL-101(Cr)
Carbamazepine
Z-scheme
Photodegradation

ABSTRACT

A series of direct Z-scheme $\alpha\text{-Fe}_2\text{O}_3/\text{MIL}-101(\text{Cr})$ hybrids were successfully prepared through a facile hydrothermal method in this work. And, the materials were characterized by some technologies including X-ray diffraction (XRD), scanning electron microscopy (SEM), energy-dispersive X-ray spectroscopy (EDX), transmission electron microscopy (TEM), Fourier-transform infrared spectroscopy (FT-IR), X-ray photoelectron spectroscopy (XPS), N₂ adsorption-desorption, photoluminescence (PL) spectroscopy, Ultraviolet-visible (UV-vis) diffuse reflectance spectroscopy (DRS) and electron spin resonance (ESR). The photocatalytic activities of the hybrids were evaluated by degradation of carbamazepine (CBZ) under visible light irradiation. It is found that 100% of CBZ was able to be removed after 180 min irradiation over the optimum $\alpha\text{-Fe}_2\text{O}_3$ (0.3)/MIL-101(Cr) hybrid. The superior activity was engendered from good textural properties and the formation of a direct Z-scheme heterojunction in the hybrid. The decomposition process of CBZ and the formation of intermediate products were analyzed through liquid chromatography-tandem mass spectrometry (LC-MS) and a possible photodegradation pathway of the CBZ was proposed. Also, the possible mechanism for the photodegradation process was provided to illustrate the excellent performance. The work has paved a new way for the application of MOF materials in the design of efficient Z-scheme system for organic pollution degradation in wastewater.

1. Introduction

Pharmaceutical product contaminants originated from the industrial effluents have gradually become a serious environmental problem and triggered increasing attention due to their high toxicity, solubility and persistence during wastewater treatment processes [1]. Among various pharmaceuticals, carbamazepine (CBZ), bearing a stable chemical structure and large consumptions, is a common psychiatric drug and used as an antiepileptic drug for a schizophrenia therapy [2]. It continuously enters into environment through different pathways. In some cases, a small amount of CBZ has strongly toxic influence on the digestive system. Moreover, the long-term intake of CBZ may cause some severe symptoms [3]. However, CBZ is a non-biodegradable organic pollutant and hard to be eliminated. Therefore, the removal of CBZ from wastewater is urgently required. Recently, photocatalytic degradation by utilizing sunlight has attracted wide attention in virtue of cost-effective, nontoxic, easily available, environmental friendly, etc [4–9]. The bottle problems of the strategy, however, are still existed in the preparation of highly effective photocatalyst with high light

harvesting, the rapid separation of photogenerated carriers and favourable surface redox reactions. Consequently, it has captured widespread interest in searching for new photocatalysts with improved photocatalytic activities.

Metal-organic frameworks (MOFs) are currently of great interest and importance because of their features, including ultrahigh surface area, well-ordered porous structures, tailororable porosity and tunable composition [10–12]. These unique properties endow MOFs with wide applications in the areas of catalysis, separations, molecular recognition, and gas storage, etc [13–15]. Also, MOF materials as potential candidates are applied into the degradation processes of pollutants in the wastewater [16]. However, some disadvantages of MOFs, including low photoresponsivity, low efficiency of visible light utilization and fast recombination of photogenerated electron-hole pairs limit their application in photocatalysts [17]. To further improve the photocatalytic activities of MOFs, many researchers coupled MOFs with some semiconductor materials (e.g., TiO₂ [18], CdS [19] and Fe₃O₄ [20]) to form hybrid materials provided with good light absorption and photocatalytic efficiency. In addition, it is found, among a variety of

* Corresponding author.

E-mail address: suyanliu@ysu.edu.cn (S. Liu).

photocatalytic systems, a direct Z-scheme photocatalytic system is deemed to be an effective way due to high separation efficiency of photogenerated electron-hole pairs [21,22]. Moreover, the Z-scheme system can obtain a high conduction band from one material and a low valence band from another material to avoid the difficult irradiation of materials with high bandgaps and enhance photocatalysis activities [23]. Obviously, it is helpful for the MOFs generally having high bandgap. Xie et al. [24] successfully constructed a Z-scheme system through combining MIL-101(Fe) with Ag_3PO_4 and observed good photocatalytic performance of antibiotics degradation. Zhou et al. [25] prepared a $\text{g-C}_3\text{N}_4/\text{NH}_2\text{-MIL-125}$ Z-scheme photocatalyst, which greatly boosted the separation of photogenerated electron-hole pairs and improved photocatalytic activities.

MIL-101(Cr), a Cr-based MOF synthesized by Férey et al. [26], has mesosized cages with microporous windows [27], giving rise to a high surface area. It exhibits prominent characteristics of large surface area, high electrical conductivity, well-ordered porous structures and channels [28]. The three dimensional structure is thought to be beneficial to charge transfer [29]. Zhou et al. [30] found that the three-dimensional structure of MIL-101(Cr) facilitated electron transfer and enhanced the photocatalytic degradation performance of Rhodamine B under visible-light. In addition, the MIL-101(Cr) has been widely used in the field of heterogeneous catalysis [31] and photocatalysis processes [32]. Unfortunately, it has a large band gap, inevitably decreasing the photocatalytic efficiency owing to difficult photogenerations of electron-hole pairs. It is well known, $\alpha\text{-Fe}_2\text{O}_3$, an n-type semiconductor with a narrow band gap, is a potential visible light driven photocatalyst due to its low cost, thermodynamical stability, and environment-friendly feature [33]. Thus, coupling strategy of $\alpha\text{-Fe}_2\text{O}_3$ with another semiconductor having suitable bandgap energy can greatly improve the photocatalytic activities of the composite material [34–36]. Ajayan et al. [37] reported a hybrid $\alpha\text{-Fe}_2\text{O}_3/2\text{D g-C}_3\text{N}_4$, exhibiting a good photocatalytic activity. The enhanced performance of the $\alpha\text{-Fe}_2\text{O}_3/2\text{D g-C}_3\text{N}_4$ is attributed to a Z-scheme structure, suppressing the electron-hole recombination in both $\alpha\text{-Fe}_2\text{O}_3$ and 2D $\text{g-C}_3\text{N}_4$. However, the $\alpha\text{-Fe}_2\text{O}_3$ possesses the disadvantage of limited accessible surface area [38]. Thus, in order to enhance the photocatalytic performances of catalysts, complementary advantages of both MIL-101(Cr) and $\alpha\text{-Fe}_2\text{O}_3$ need to be integrated.

Herein, we have combined MIL-101(Cr) with $\alpha\text{-Fe}_2\text{O}_3$ to form a direct Z-scheme $\alpha\text{-Fe}_2\text{O}_3/\text{MIL-101}(\text{Cr})$ hybrid with enhancing photocatalytic activity through a facile hydrothermal method. To the best of our knowledge, the work that the hybrid $\alpha\text{-Fe}_2\text{O}_3/\text{MIL-101}(\text{Cr})$ is prepared and utilized in the photodegradation process of organic pollutants has not been reported. In the paper, the photocatalytic activities of $\alpha\text{-Fe}_2\text{O}_3/\text{MIL-101}(\text{Cr})$ hybrids were systematically evaluated by the degradations of CBZ under visible light irradiation. The identified experiments for active radicals and electron spin resonance (ESR) analysis were conducted to explore a possible degradation mechanism for the CBZ. And, the reusability test of the hybrid $\alpha\text{-Fe}_2\text{O}_3/\text{MIL-101}(\text{Cr})$ was also performed.

2. Experimental

2.1. Materials

All the chemicals were analytical grades and used without further purification. Chromic nitrate hydrate (99%, $\text{Cr}(\text{NO}_3)_3 \cdot 9\text{H}_2\text{O}$) and $\text{FeCl}_3 \cdot 6\text{H}_2\text{O}$ were purchased from the Aladdin Industrial Corporation (Shanghai, China). Terephthalic acid (TPA, 99%) was supplied by J&K Scientific Ltd. (Beijing, China). Hydrofluoric acid (HF, 40%) was purchased from Kaitong Chemical Reagent Co. Ltd. (Tianjin, China). Deionized water ($18.0\text{ M}\Omega\text{ cm}$) was used in all experiments.

2.2. Synthesis of MIL-101(Cr)

MIL-101(Cr) was synthesized according to a literature [39]. The

synthesis procedure was described as follow. Terephthalic acid (1.1067 g) was firstly added into deionized water (30 mL) in a plastic flask, and then they were continuously stirred at room temperature for 15 min. 2.67 g of $\text{Cr}(\text{NO}_3)_3 \cdot 9\text{H}_2\text{O}$ was further added into the plastic flask under a steady stirring-rate condition. After the forming mixture was stirred again for 20 min, 0.45 mL of HF was introduced into the synthesis system, following with another 1 h stirring. The final mixture was transferred into a Teflon lined autoclave (50 mL) and was heated to 220 °C for 8.5 h. Then, a solid product with a green colour was recovered by filtration. In order to purify it, a three-step procedure was carried out. Firstly, the solid product was filtered, washed to neutrality by using ethanol (60 °C) and deionized water (80 °C), respectively and dried at 100 °C for 2 h. Secondly, the treated solid product was introduced into 150 mL of ethanol again with stirring magnetically at 60 °C for 12 h, and it was further filtered and dried at 60 °C overnight. Finally, the dried product was washed with 150 mL of water and stirred magnetically at 80 °C for 12 h, and then it was filtered and dried at 60 °C overnight. The final purified product MIL-101(Cr) was obtained through dehydrating at 150 °C overnight and stored in the desiccators for future use.

2.3. Preparation of $\alpha\text{-Fe}_2\text{O}_3/\text{MIL-101}(\text{Cr})$

0.15 g of the MIL-101(Cr) was added into 30 mL of deionized water and was stirred magnetically at room temperature for 15 min to form a mixture. $\text{FeCl}_3 \cdot 6\text{H}_2\text{O}$ with a certain amount was dissolved in the mixture and was stirred again for 30 min. Then, the mixture was transferred into a Teflon lined autoclave and was heated to 140 °C for 24 h. Next, a hybrid was obtained through filtration, washing with water and drying at 60 °C overnight. The obtain hybrid was denoted as $\alpha\text{-Fe}_2\text{O}_3(\text{C})/\text{MIL-101}(\text{Cr})$, where C represents 0.1, 0.2, 0.3, 0.4 and 0.5 g according to the introduction amount of $\text{FeCl}_3 \cdot 6\text{H}_2\text{O}$, respectively.

2.4. Characterization

X-ray diffraction (XRD) patterns were obtained on a Bruker D8 Advance X-ray diffractometer in the range of $2\theta = 5\text{--}80^\circ$ using Cu K α radiation. Scanning electron microscopy equipped with an energy-dispersive X-ray spectroscopy (SEM-EDS; S-4800 field-emission) was applied at 10 kV on samples that were gold sputtered before analysis. The morphological analysis of the samples was investigated by transmission electron microscopy (TEM, HT7700) at 100 kV. The high resolution transmission electron microscopy (HRTEM, Tecnai G2 F20) was carried out to clarify the microstructures of the samples. Fourier-transform infrared (FT-IR) spectra were detected the surface functional groups using a Nicolet IS 10 spectrometer. The element states of the samples were analyzed using a Thermo Escalab 250XI X-ray photoelectron spectroscope (XPS) using Al K α radiation, calibrating binding energies using the C 1s peak (284.8 eV) from carbon contamination. Nitrogen adsorption-desorption isotherms were conducted at 77 K by N_2 physisorption on a Micromeritics ASAP2020 analyzer. The specific surface area was calculated by the Brunauer-Emmett-Teller (BET) method. The pore size distribution was analyzed by the non-local density functional theory (NL-DFT) method. The photoluminescence (PL) spectra were measured using a Hitachi F-7000 fluorescence spectrophotometer. The excitation wavelength and emission wavelength for all samples is 300 nm and 320 nm, respectively. The UV-vis diffuse reflectance spectroscopy (DRS) was carried out in a Shimadzu UV-2700 spectrophotometer with BaSO_4 as reference. The JEOL FA-300 instrument was used to obtain the electron spin resonance (ESR) signals of the spin trapped oxidative radicals with the spin-trapping agent 5,5-dimethyl-1-pyrroline-N-oxide (DMPO).

2.5. Photocatalytic experiments

The photocatalytic activity of a sample was evaluated by

degradation of carbamazepine (CBZ) solution under visible light irradiation. The solution was illuminated vertically using a 300-W Xe lamp (PLS-SXE300UV, Beijing Perfect Light Co., Ltd.) with a UV cut-off filter ($\lambda \geq 420$ nm). Degradation of CBZ was performed in a 100 mL glass reactor with an ice bath to maintain the solution at 0 °C. CBZ solution (50 mL, 30 mg L⁻¹) mixed with 10 mg photocatalyst was placed into the glass reactor, following by the addition of 100 µL H₂O₂ into the mixture solution. Before a photocatalytic measurement was carried out, the mixed solution was continuously stirred in dark condition for 60 min to achieve adsorption-desorption equilibrium. A sample used as a dark control was wrapped with aluminum foil and kept in dark environment. At a regular interval of time, 3 mL of the suspension was collected and immediately centrifuged to remove the photocatalysts. The absorption spectrum of the treated CBZ aqueous solution was obtained by UV-vis spectrophotometer at $\lambda_{\text{max}} = 285$ nm.

2.6. Electrochemical measurements

Electrochemical measurements were performed using a three-electrode system connected to an electrochemical workstation (CHI760, CH Instruments) and carried out in a chemical bath using 0.1 M KCl as electrolyte. The working electrode was a Glassy-Carbon Electrode (GCE) (diameter: 3 mm) with a PTFE coater, which was polished and cleaned with deionized water. After that, the electrode was thoroughly rinsed with deionized water. Here, Ag/AgCl and platinum plate was used as reference and counter electrodes, respectively. Detailedly, the working electrode was prepared as following procedure. 10 mg of photocatalyst powder was dispersed in 5 mL ethanol, and then 20 µL of Nafion solution was added. The suspension was immersed in an ultrasonic bath for 30 min to prepare homogeneous mixing suspension. The working electrode was prepared by depositing 20 µL mixed solution onto GCE. The Mott-Schottky analysis with frequencies of 1000 Hz and amplitude of 1 mV was conducted. All experiments were performed at ambient temperature and the measured potentials versus Ag/AgCl were converted to the reversible hydrogen electrode (RHE), calculating by the equation $E_{\text{RHE}} = E_{\text{Ag/AgCl}} + 0.059 \times \text{pH} + 0.197$.

2.7. Chemical analysis

The concentration of sampled CBZ was quantified by a high-performance liquid chromatography (HPLC, Agilent 1290 series) equipped with a diode array detector and C18 column (150 mm × 2.1 mm × 1.8 µm; Eclipse Plus C18). The temperature of the column compartment was set as 25 °C and the detection wavelength was 285 nm. The acetonitrile and ultrapure water solution with 0.1% formic acid and 0.5 mM ammonium acetate were used as the mobile phase, with a flow rate of 0.3 mL min⁻¹. Products were identified by a mass spectrometer LC-MS system. Mass spectrometry was carried out using an Agilent Technologies 6460 Triple Quad LC/MS system equipped with electrospray ionization (ESI) source. The positive ionization mode was applied and analyzed by an *m/z* range of 50–350.

3. Results and discussion

3.1. Material characterization

The crystal structures of as-prepared samples were probed by X-ray diffraction patterns (XRD). As shown in Fig. 1a, characteristic diffraction peaks exhibited in MIL-101(Cr) are in agreement with reports in some previous literatures [40,41]. According to JCPDS (33-0664), peak presented at $2\theta = 24.1, 33.1, 35.6, 40.8, 49.5, 54.1, 57.6, 62.4, 64, 71.9$ and 75.4° can be indexed as (012) (104) (110) (113) (024) (116) (018) (214) (300) (1,0,10) and (220) crystal planes of α-Fe₂O₃ (see Fig. 1g), respectively. It can be clearly observed that the XRD patterns of α-Fe₂O₃(C)/MIL-101(Cr) hybrids all exhibit the characteristic peaks of both MIL-101(Cr) and α-Fe₂O₃, confirming that the hybrids have

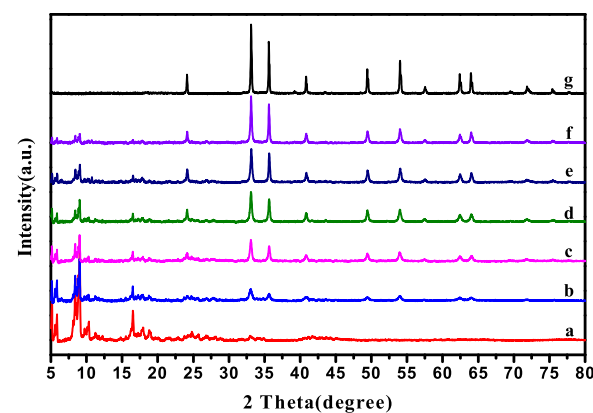


Fig. 1. XRD patterns of samples: (a) MIL-101(Cr), (b)-(f) α -Fe₂O₃(C)/MIL-101(Cr) (C is 0.1, 0.2, 0.3, 0.4 and 0.5, respectively) and (g) α -Fe₂O₃.

been successfully prepared. It is noteworthy that the diffraction peak intensities of α -Fe₂O₃ phases are gradually enhanced in the hybrids with increasing the introduction amounts of α -Fe₂O₃, while those of MIL-101(Cr) phases are weakened. Furthermore, considering that the Scherrer's equation cannot always calculate accurately the actual size due to possible crystal defects, the crystal growth tendencies of the α -Fe₂O₃ phases in the hybrids are discussed by the full widths at half maximum (FWHM). As reducing the amounts of α -Fe₂O₃ from 0.5 to 0.1 g, the diffraction peaks for the α -Fe₂O₃ phases are broaden in the hybrids (see Fig. 2) and the FWHM of (104) and (110) peaks are also gradually increased (see Table 1), illustrating the hybrids bearing smaller particle sizes compared to those of the pure α -Fe₂O₃.

The morphologies and particle sizes of the as-prepared samples were characterized by SEM. It can be seen from Fig. 3a, the MIL-101(Cr) presents an octahedral structure [42–45], while a pure α -Fe₂O₃ exhibits uniform spherical particles (see Fig. 3b). In Fig. 3c, distinct phenomenon is observed that α -Fe₂O₃ spherical particles are attached to the surface of the MIL-101(Cr). Based on scales of SEM images (see Fig. 3a and b), the average diameter of the MIL-101(Cr) and α -Fe₂O₃ is about 680 nm and 420 nm, respectively. Compared with the pure α -Fe₂O₃, the α -Fe₂O₃ in the hybrid α -Fe₂O₃(0.3)/MIL-101(Cr) had smaller average particle sizes, indicating that the formation and growth of the phase α -Fe₂O₃ was influenced by the interaction between the both phases during the preparation process. The composition of the α -Fe₂O₃(0.3)/MIL-101(Cr) was further analyzed by EDX. As shown in Fig. 3d–g, Cr, C, Fe, and O elements all appear in the hybrid. The results also provide evidence for the XRD argument of simultaneous presence of MIL-101(Cr) and α -Fe₂O₃ phases. Moreover, it can also be seen from the EDX images that element Cr, C, Fe and O derived from MIL-101(Cr) and

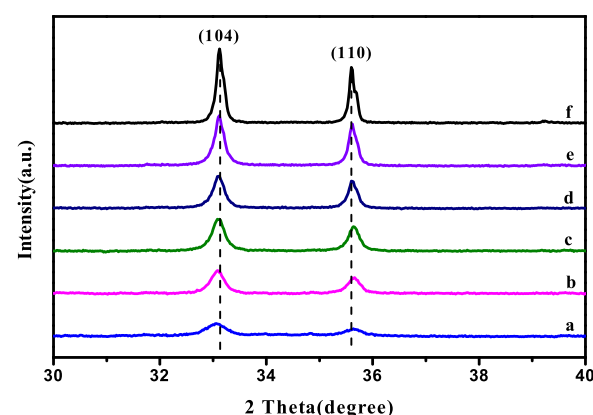


Fig. 2. XRD patterns of samples: (a)-(e) α -Fe₂O₃(C)/MIL-101(Cr) (C is 0.1, 0.2, 0.3, 0.4 and 0.5, respectively) and (f) α -Fe₂O₃.

Table 1

FWHM of diffraction peaks of different samples.

Peak	$\alpha\text{-Fe}_2\text{O}_3(0.1)/\text{MIL-101(Cr)}$	$\alpha\text{-Fe}_2\text{O}_3(0.2)/\text{MIL-101(Cr)}$	$\alpha\text{-Fe}_2\text{O}_3(0.3)/\text{MIL-101(Cr)}$	$\alpha\text{-Fe}_2\text{O}_3(0.4)/\text{MIL-101(Cr)}$	$\alpha\text{-Fe}_2\text{O}_3(0.5)/\text{MIL-101(Cr)}$	$\alpha\text{-Fe}_2\text{O}_3$
(104)	0.414	0.319	0.299	0.263	0.222	0.162
(110)	0.316	0.280	0.267	0.224	0.188	0.142

$\alpha\text{-Fe}_2\text{O}_3$ are uniformly distributed in the hybrid.

TEM images of samples are provided in Fig. 4. The results also agree that MIL-101(Cr) and $\alpha\text{-Fe}_2\text{O}_3$ has the regular crystal morphology and spherical particles, respectively (see Fig. 4a, b). Those are basically consistent with those of SEM. Also, the behavior of the $\alpha\text{-Fe}_2\text{O}_3$ uniformly anchored onto the surface of MIL-101(Cr) is clearly observed in Fig. 4c. In addition, the fact, the $\alpha\text{-Fe}_2\text{O}_3$ in the hybrid bearing smaller particle sizes compared to those of the pure $\alpha\text{-Fe}_2\text{O}_3$ is confirmed again, which is in accordance with the results of the XRD and SEM. Smaller particle sizes are beneficial to make improvements in surface area and surface active sites. High-resolution transmission electron microscopy (HRTEM) images (see Fig. 4d and Fig. S1) exhibit that some micro-porous structures are clearly detected in MIL-101(Cr). It can also be seen from Fig. 4e, f and Fig. S2, 3, the $\alpha\text{-Fe}_2\text{O}_3$ in the hybrid is provided with a lattice spacing of about 0.25 nm, which is identical with that of the pure $\alpha\text{-Fe}_2\text{O}_3$. As shown in Fig. 4f, a distinct interface between $\alpha\text{-Fe}_2\text{O}_3$ and MIL-101(Cr) phases is observed to appear in the hybrid, which further indicates the successful combination and the construction of an excellent interface interaction between the both phases.

The FT-IR spectra in Fig. 5 clearly state that the skeleton vibration structures of the MIL-101(Cr) and $\alpha\text{-Fe}_2\text{O}_3$ phases all exist in the hybrids. Characteristic vibration bands at around 1403 and 1504 cm⁻¹ for the framework (O-C-O)- group confirm the presence of the dicarboxylate moieties in MIL-101(Cr), while an broad peak at 475 cm⁻¹ may be ascribed to Fe-O bond originated from the phase $\alpha\text{-Fe}_2\text{O}_3$ and its intensity gradually enhances with the increasing amounts of $\alpha\text{-Fe}_2\text{O}_3$. It proves the existence of phase $\alpha\text{-Fe}_2\text{O}_3$ in the hybrid again. These results are also in good agreement with those of the XRD, SEM and TEM measurements.

The surface elemental compositions and valence states in samples were determined by X-ray photoelectron spectroscopy (XPS) technology. The XPS survey spectrum in Fig. 6a exhibits evidence that element Cr, Fe, C, and O are indeed in the hybrid $\alpha\text{-Fe}_2\text{O}_3(0.3)/\text{MIL-101(Cr)}$.

101(Cr), which coincides with the observation from SEM-EDX and TEM-EDS. To further prove the interaction between MIL-101(Cr) and $\alpha\text{-Fe}_2\text{O}_3$, high-resolution XPS spectra of Cr 2p, Fe 2p, C 1s, and O 1s were investigated. As shown in Fig. 6b, Cr 2p1/2 and Cr 2p3/2 peaks located at 587.2 and 577.6 eV imply the existence of Cr-O [46]. Fe 2p in the pure $\alpha\text{-Fe}_2\text{O}_3$ (see Fig. 6c) is detected at 711.7 and 725.1 eV, which can be assigned to Fe 2p3/2 and Fe 2p1/2 peaks in the phase $\alpha\text{-Fe}_2\text{O}_3$, respectively. The binding energies of Fe 2p originated from $\alpha\text{-Fe}_2\text{O}_3$ in the hybrid are slightly shifted to lower binding energies compared to that of the pure $\alpha\text{-Fe}_2\text{O}_3$. The C 1s spectrum of the pure MIL-101(Cr) (see Fig. 6d) exhibits peaks centred at 284.3, 284.8 and 285.6 eV, which are produced from C-C, C=O and C-O bonds. Simultaneously, the binding energies of C 1s in the hybrid have distinct shifts toward higher binding energies compared to those of MIL-101(Cr). In Fig. 6e and f, the O 1s spectrum of the hybrid is fitted into three peaks. The peak at 529.9 eV represents characteristics of oxygen species in the $\alpha\text{-Fe}_2\text{O}_3$, the peak of 531.9 eV can be ascribed to the oxygen atom in the forms of -COOH bonds, while the peak around 533.3 eV is bred from surface molecular water [47,48]. Similarly, compared with $\alpha\text{-Fe}_2\text{O}_3$ and MIL-101(Cr), the binding energies of O 1s for the $\alpha\text{-Fe}_2\text{O}_3/\text{MIL-101(Cr)}$ are also observed to basically shift to higher binding energies. These shifts prove the interfacial interaction between both MIL-101(Cr) and $\alpha\text{-Fe}_2\text{O}_3$. The view can be supported by Jiang's paper [23].

The nitrogen adsorption-desorption isotherms of MIL-101(Cr), $\alpha\text{-Fe}_2\text{O}_3(0.3)/\text{MIL-101(Cr)}$ and $\alpha\text{-Fe}_2\text{O}_3$ are shown in Fig. 7a. The isotherm of MIL-101(Cr) basically exhibits characteristics of type I, bearing an obvious hysteresis loop at $P/P_0 = 0.2\text{--}0.3$, which indicates the simultaneous presence of porous structures in the material. The result is further proved by pore size distribution curves of the material calculated from NL-DFT models. The MIL-101(Cr) presents hierarchical porous structures with different pore sizes of 1.30, 1.94 and 2.40 nm, as shown in Fig. 7b. However, the isotherm of $\alpha\text{-Fe}_2\text{O}_3$ may be categorized as type III, appearing the adsorption behavior of a non-porous material.

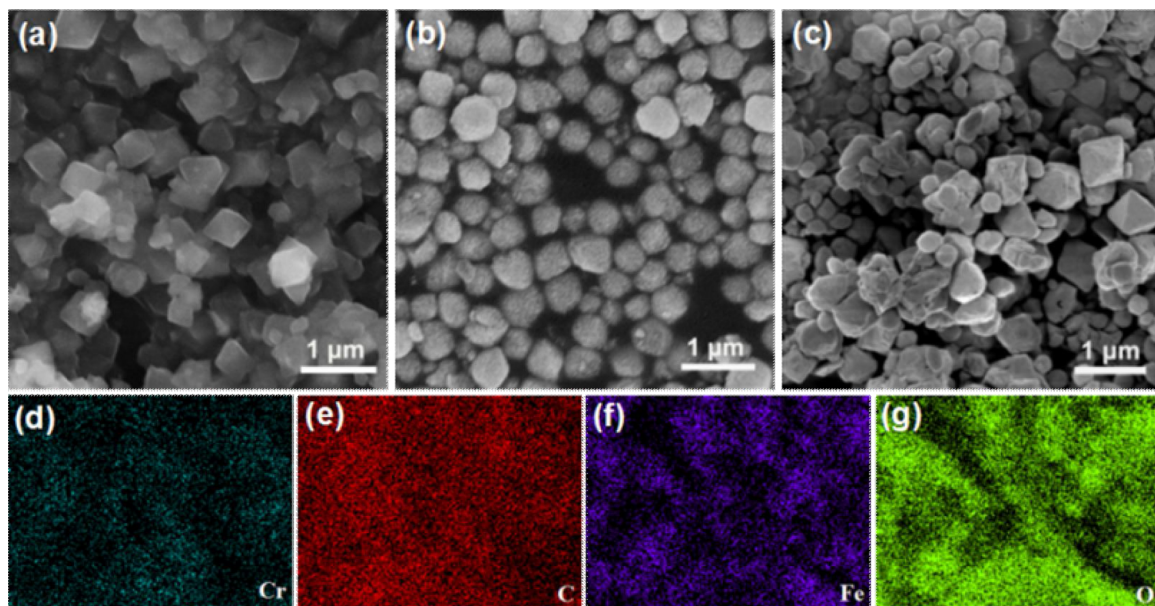


Fig. 3. SEM images of (a) MIL-101(Cr), (b) $\alpha\text{-Fe}_2\text{O}_3$, (c) $\alpha\text{-Fe}_2\text{O}_3(0.3)/\text{MIL-101(Cr)}$, elemental mapping images of (d) Cr, (e) C, (f) Fe and (g) O.

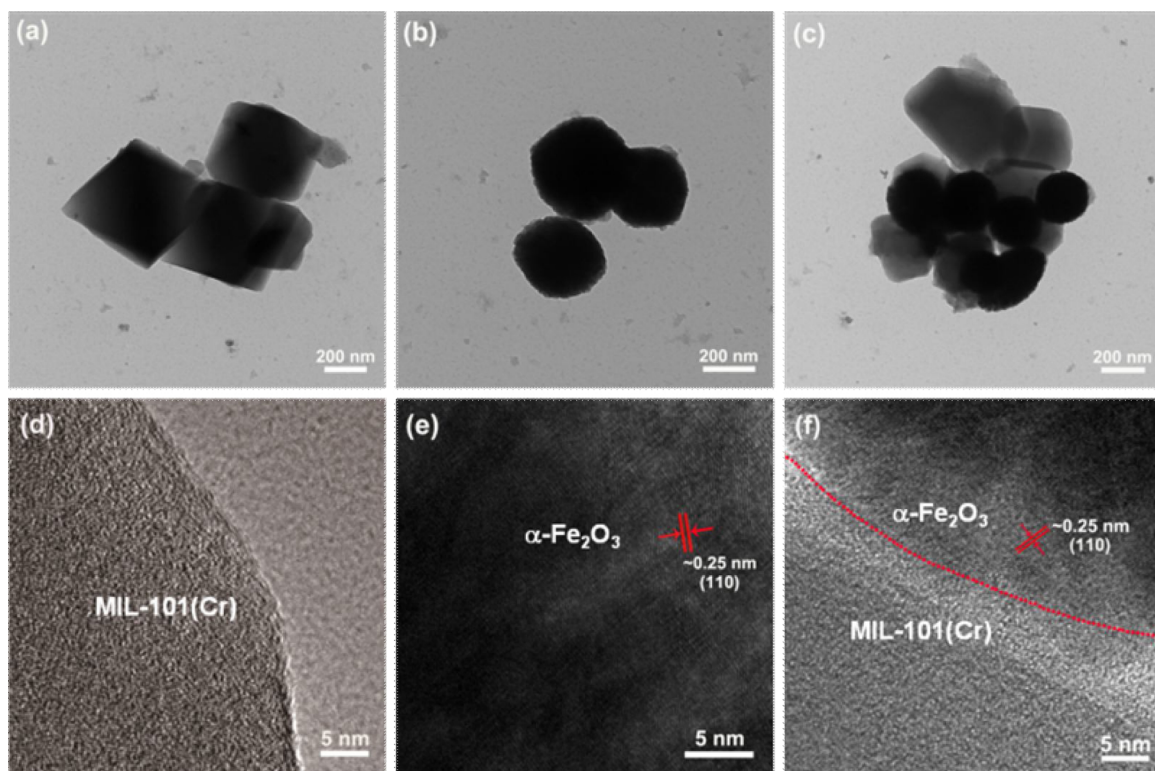


Fig. 4. TEM images of (a) MIL-101(Cr), (b) α -Fe₂O₃, (c) α -Fe₂O₃(0.3)/MIL-101(Cr), HRTEM images of (d) MIL-101(Cr), (e) α -Fe₂O₃ and (f) α -Fe₂O₃(0.3)/MIL-101(Cr).

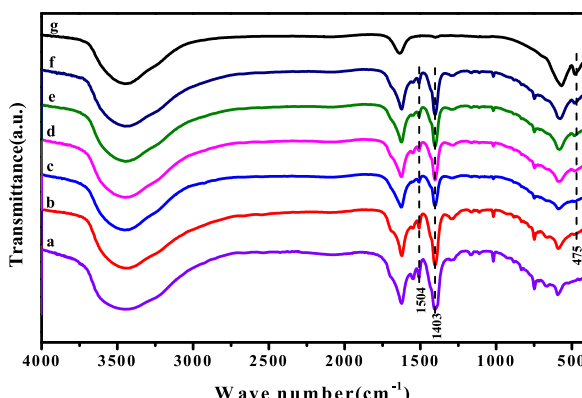


Fig. 5. FT-IR spectra of (a) MIL-101(Cr), (b)-(f) α -Fe₂O₃(C)/MIL-101(Cr) (C is 0.1, 0.2, 0.3, 0.4 and 0.5, respectively) and (g) α -Fe₂O₃.

The α -Fe₂O₃(0.3)/MIL-101(Cr) inherits and integrates features of the both, resulting in an intermediate adsorption volume compared to those of MIL-101(Cr) and α -Fe₂O₃. Also, pore sizes of 1.30, 1.94 and 2.40 nm were formed in the α -Fe₂O₃(0.3)/MIL-101(Cr). Table 2 listed surface area calculating from BET model and pore volumes of MIL-101(Cr), α -Fe₂O₃(0.3)/MIL-101(Cr) and α -Fe₂O₃. Compared with the BET surface area ($2518.0\text{ m}^2\text{ g}^{-1}$) and pore volume ($1.355\text{ cm}^3\text{ g}^{-1}$) of MIL-101(Cr), the α -Fe₂O₃(0.3)/MIL-101(Cr) obtains low those ($948.6\text{ m}^2\text{ g}^{-1}$ and $0.559\text{ cm}^3\text{ g}^{-1}$, respectively), however, which are significantly higher than those of the α -Fe₂O₃ (only $6.558\text{ m}^2\text{ g}^{-1}$ and $0.024\text{ cm}^3\text{ g}^{-1}$, respectively). Large pore sizes, high surface area and pore volume of the hybrid provide more active adsorption sites and reaction space, facilitating the diffusion of macromolecules and accessibility of active sites, which is beneficial to the enhancement of photocatalytic performances.

The separation nature of photogenerated electron-hole pairs was studied by photoluminescence (PL) emission intensity. As shown in Fig. 8, the emission peak of α -Fe₂O₃/MIL-101(Cr) is remarkably

weakened in comparison with that of pure MIL-101(Cr), the PL peak intensity of MIL-101(Cr) is greatly decreased after combination with α -Fe₂O₃. It implies the formations of synergistic effects between MIL-101(Cr) and α -Fe₂O₃, which suppress photogenerated electron-hole pairs recombination and boost interfacial charge transferring.

The optical properties of the MIL-101(Cr), α -Fe₂O₃(0.3)/MIL-101(Cr) and α -Fe₂O₃ were analyzed by UV-vis diffuse reflectance spectra (DRS). It can be seen from Fig. 9, the MIL-101(Cr) exhibits visible-light absorption with wavelength shorter than 370 nm, however, the hybrid shows a high absorbance in the visible light range after α -Fe₂O₃ loading, indicating that the introduction of α -Fe₂O₃ can extend visible light absorption ability. Moreover, the band gap value of α -Fe₂O₃ is estimated to be 2.02 eV. The calculated band gaps derived from the Tauc plot (see Fig. 9b) of the hybrids are all lower than that of the MIL-101(Cr) (3.62 eV), which presents evidence that the introduction of α -Fe₂O₃ narrows the band gap of the hybrid. It is helpful for the generation of photodegradation carriers.

3.2. Photocatalytic activity

CBZ adsorption equilibrium curves over α -Fe₂O₃, α -Fe₂O₃/MIL-101(Cr) and MIL-101(Cr) in the dark control experiments were presented in Fig. S5. It can be seen from the curves that all adsorption processes reach equilibrium after 60 min, removing a small amount of CBZ. The photocatalytic activities of samples were further evaluated by degradations of CBZ under visible light ($\lambda \geq 420\text{ nm}$) irradiation. As shown in Fig. S6, it can be observed that the intensity of characteristic absorption peak at $\sim 285\text{ nm}$ steadily decreases with exposure time increasing in the photodegradation process of CBZ. And, the photocatalytic activities of the different catalysts under visible light irradiation are presented in Fig. 10. The result illustrates that all hybrids exhibit higher photodegradation rate than those of the pure MIL-101(Cr) and α -Fe₂O₃. Also, some phenomenon can be observed, the photodegradation efficiency of CBZ is gradually increased when the

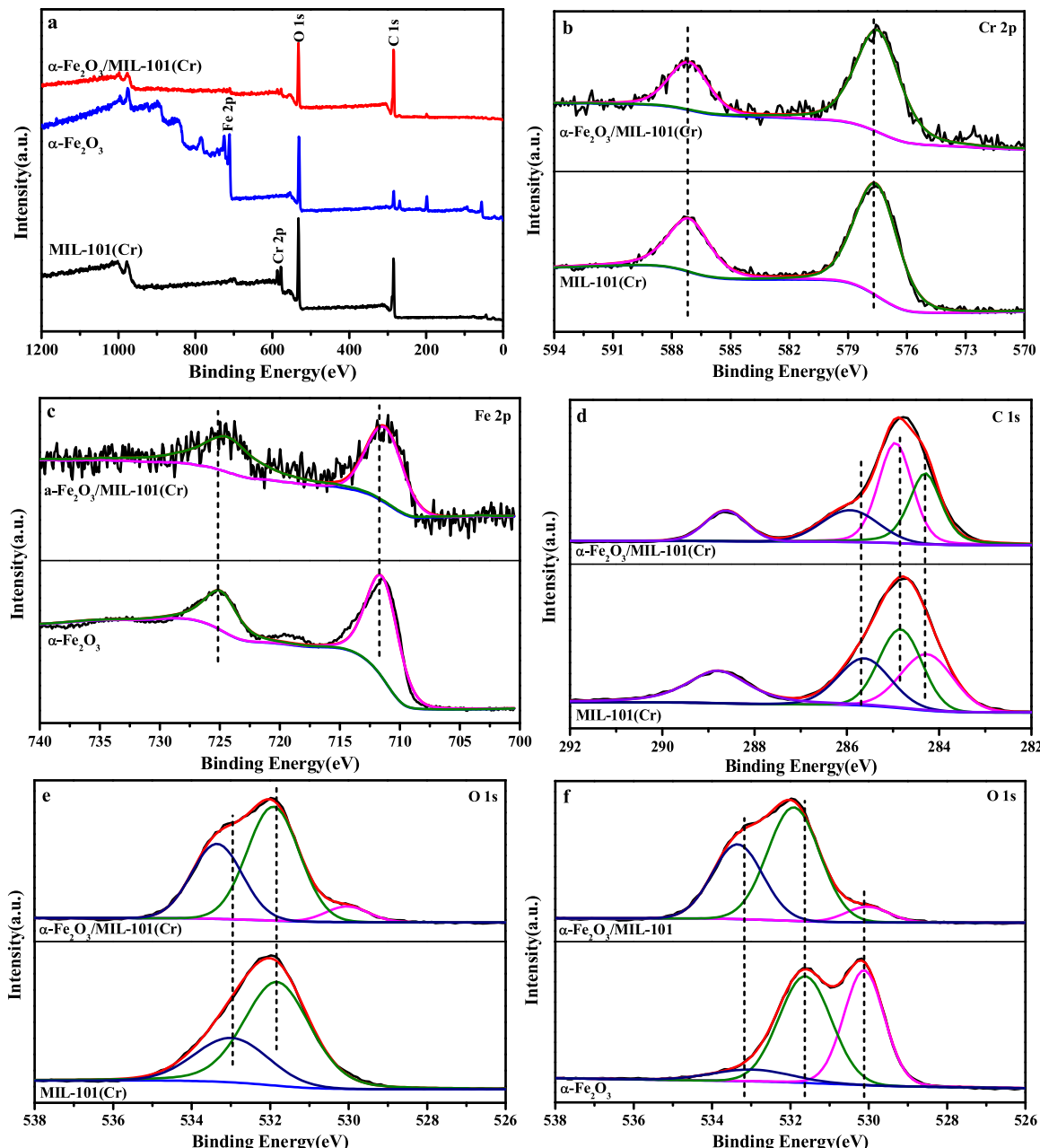


Fig. 6. (a) XPS survey spectrum of $\alpha\text{-Fe}_2\text{O}_3(0.3)/\text{MIL-101}(\text{Cr})$, high-resolution XPS spectra of (b) Cr 2p, (c) Fe 2p, (d) C 1s, (e) and (f) O 1s.

introduction amount of $\alpha\text{-Fe}_2\text{O}_3$ is increased from 0.1 to 0.3 g. Interestingly, the contrary tendency for the removing rate of CBZ is observed as the introduction amount of $\alpha\text{-Fe}_2\text{O}_3$ is further increased to 0.5 g. As is known to all, the $\alpha\text{-Fe}_2\text{O}_3$ with a low bandgap easily generates electron-hole pairs under visible light irradiation. Thus, appropriate introduction amounts of $\alpha\text{-Fe}_2\text{O}_3$ into the hybrid may accelerate the separation of electron-hole pairs and improve the degradation performance thanks to the interaction between MIL-101(Cr) and $\alpha\text{-Fe}_2\text{O}_3$. Unfortunately, the introduction of excessive $\alpha\text{-Fe}_2\text{O}_3$ brings about disadvantages for the textural properties of the hybrids, leading to the low photo-degradation activity, especially for the pure $\alpha\text{-Fe}_2\text{O}_3$ bearing the lowest photocatalytic performance. It's worth noting, all hybrids exhibit higher photocatalytic activity than those of the pure MIL-101(Cr) and $\alpha\text{-Fe}_2\text{O}_3$. Furthermore, compared with a mechanical mixture bearing the same introduction amount of $\alpha\text{-Fe}_2\text{O}_3$, the hybrid $\alpha\text{-Fe}_2\text{O}_3(0.3)/\text{MIL-101}(\text{Cr})$ exhibits a superior photocatalytic activity for the CBZ with 100% degradation rate within 180 min, indicating the interaction plays an

important role in the degradation of CBZ process.

In order to understand the reaction kinetics of the photocatalytic degradation of CBZ, the reaction rate constant k was calculated from the following equation and this process followed with the pseudo first order reaction:

$$\ln (C_t / C_0) = -kt$$

Where, C_0 and C_t is the concentrations of the CBZ solution at time 0 and t , respectively. As shown in Fig. 11, the rate constant k of CBZ degradation for the photocatalyst $\alpha\text{-Fe}_2\text{O}_3(0.3)/\text{MIL-101}(\text{Cr})$ is 0.0080 min^{-1} , which is higher than those of MIL-101(Cr) (0.0017 min^{-1}) and $\alpha\text{-Fe}_2\text{O}_3$ (0.0040 min^{-1}) photocatalysts in dark condition. Making a comparison with dark condition, the hybrid photocatalyst (0.0152 min^{-1}) presents significantly enhanced k value compared to MIL-101(Cr) (0.0021 min^{-1}) and $\alpha\text{-Fe}_2\text{O}_3$ (0.0050 min^{-1}) under visible light irradiation, demonstrating photocatalytic degradation plays a major role in the process.

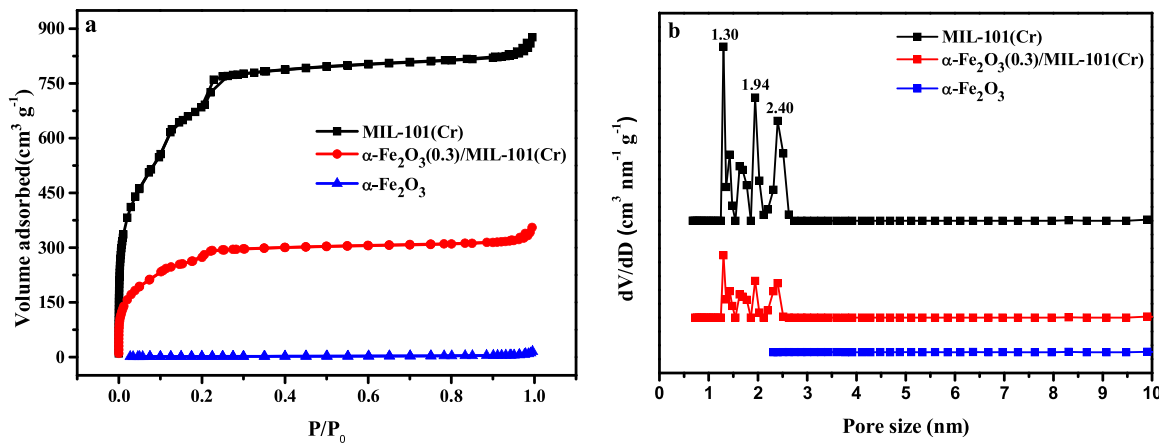


Fig. 7. (a) Nitrogen sorption isotherms of MIL-101(Cr), $\alpha\text{-Fe}_2\text{O}_3(0.3)/\text{MIL-101}(\text{Cr})$ and $\alpha\text{-Fe}_2\text{O}_3$, (b) NL-DFT pore size distribution of MIL-101(Cr), $\alpha\text{-Fe}_2\text{O}_3(0.3)/\text{MIL-101}(\text{Cr})$ and $\alpha\text{-Fe}_2\text{O}_3$.

Table 2

BET surface area and pore volumes of samples.

Sample	S_{BET} ($\text{m}^2 \text{g}^{-1}$)	S_{mic} ($\text{m}^2 \text{g}^{-1}$)	S_{ext} ($\text{m}^2 \text{g}^{-1}$)	V_{mic} ($\text{cm}^3 \text{g}^{-1}$)	V_{ext} ($\text{cm}^3 \text{g}^{-1}$)	V_{total} ($\text{cm}^3 \text{g}^{-1}$)
MIL-101(Cr)	2518.0	67.1	2450.9	0.004	1.351	1.355
$\alpha\text{-Fe}_2\text{O}_3(0.3)/\text{MIL-101}(\text{Cr})$	948.6	122.1	826.5	0.060	0.499	0.559
$\alpha\text{-Fe}_2\text{O}_3$	6.558	0.917	5.641	0.001	0.023	0.024

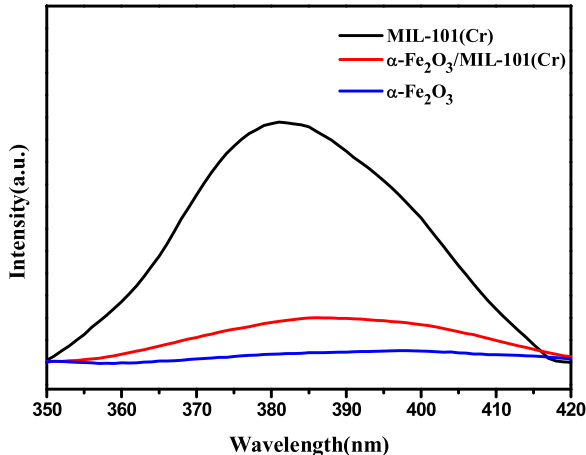


Fig. 8. PL spectra of MIL-101(Cr), $\alpha\text{-Fe}_2\text{O}_3(0.3)/\text{MIL-101}(\text{Cr})$ and $\alpha\text{-Fe}_2\text{O}_3$ photocatalysts.

The reusability of a photocatalyst is a critical issue for further applications. To investigate the reusability of the $\alpha\text{-Fe}_2\text{O}_3(0.3)/\text{MIL-101}(\text{Cr})$, the reused hybrid was centrifuged and dried at 60 °C for 12 h to remove impurities, and then it was reused in the next cycle under the same condition. It can be seen from Fig. 12, the removal rate of CBZ in the fourth cycle still retains 91%, illustrating the good reusability of the hybrid $\alpha\text{-Fe}_2\text{O}_3/\text{MIL-101}(\text{Cr})$.

3.3. CBZ degradation pathway

According to HPLC analysis results (see Fig. S7), it can be analyzed that the peak area of CBZ gradually decreases with the exposure time increasing, further indicating the superior photocatalytic activity of the $\alpha\text{-Fe}_2\text{O}_3(0.3)/\text{MIL-101}(\text{Cr})$ for the degradation of CBZ. The structures for photodegradation intermediates of CBZ ($m/z = 237 \text{ g mol}^{-1}$) over the hybrid (see Fig. S8) and possible degradation pathway are proposed in Fig. 13. First, alkene double bond of CBZ was vulnerable to be

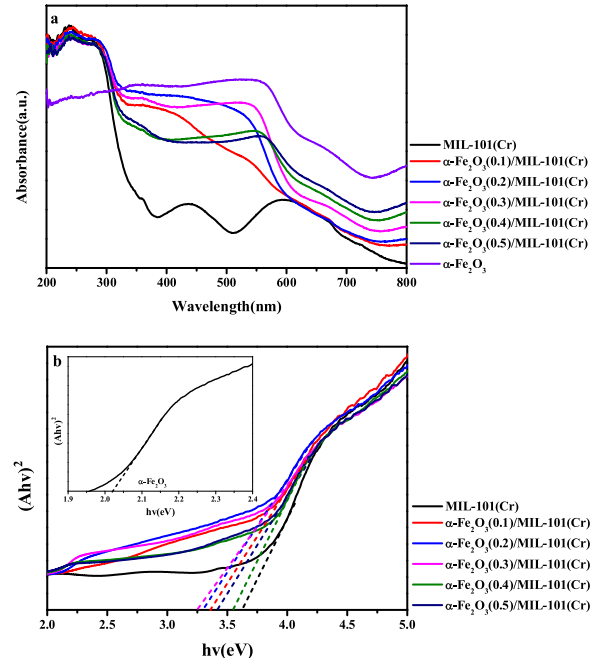


Fig. 9. (a) UV-vis DRS spectra and (b) plots of $(\text{Ahy})^2$ versus photon energy of samples.

attacked by 'OH radical because of its higher frontier electron density which was likely to conduct hydroxylation. Therefore, CBZ was transferred into intermediate P1 ($m/z = 253 \text{ g mol}^{-1}$) and P2 ($m/z = 253 \text{ g mol}^{-1}$) [49]. Besides, with the attack of the 'OH at the olefinic double bond on the central heterocyclic ring and an oxidized process by h^+ , intermediate P1 was transferred into P3 ($m/z = 275 \text{ g mol}^{-1}$). Intermediate P2 might be further oxidized by ' O_2^- ' and photoinduced h^+ to be converted into P4 ($m/z = 269 \text{ g mol}^{-1}$) and P5 ($m/z = 253 \text{ g mol}^{-1}$) [50]. Then, Intermediate P5 underwent several successive steps including deamination and dehydroxylation to generate P6 ($m/z = 180 \text{ g mol}^{-1}$)

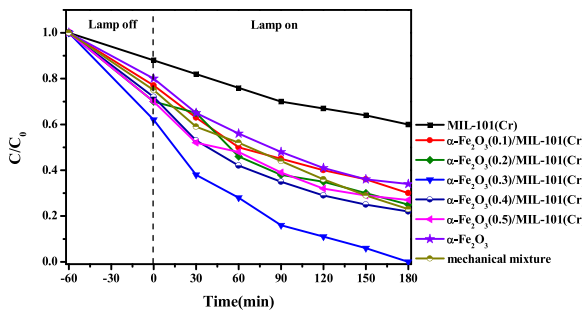


Fig. 10. Degradation efficiencies of CBZ over different photocatalysts.

mol^{-1}) [51,52]. As for intermediate P6, it reacted with $\cdot\text{OH}$ to be changed into P7 ($m/z = 195 \text{ g mol}^{-1}$). After aldehyde oxidation reaction in P4, P8 ($m/z = 301 \text{ g mol}^{-1}$) was produced and further transferred into P9 ($m/z = 259 \text{ g mol}^{-1}$), which was ascribed to deamination reaction [53]. In addition, intermediate P4 followed the intramolecular cyclization and hydrolysis of the urea group on the central heterocyclic ring to generate P10 ($m/z = 223 \text{ g mol}^{-1}$), while the intermediate P11 ($m/z = 287 \text{ g mol}^{-1}$) was formed through the rapid hydroxylation of intermediate P1 [54,55]. CBZ also accompanied a direct hydrolysis step to produce intermediate P12 ($m/z = 210 \text{ g mol}^{-1}$). It is noteworthy that all products degraded from CBZ could be further transpired as harmless CO_2 and H_2O .

3.4. Photodegradation mechanism

To investigate the photodegradation mechanism of CBZ, radical trapping experiments involving various main active oxidation species were carried out, in which potassium iodide (KI, 5 mg), n-butylalcohol (NBA, 1 mL) and nitrogen was employed as the scavengers of holes (h^+), hydroxyl radicals ($\cdot\text{OH}$) and superoxide radicals ($\cdot\text{O}_2^-$), respectively. As shown in Fig. 14, slight inhibition result of photocatalytic activity induced by the nitrogen reveals that $\cdot\text{O}_2^-$ is not a main active species in charge of the degradation of CBZ in current photocatalytic systems. However, it can be observed that the introductions of KI and NBA induce higher inhibition of photocatalytic activity compared to that of $\cdot\text{O}_2^-$. Notably, the NBA exhibits a more obvious suppressing action for the CBZ degradation, which suggests that $\cdot\text{OH}$ controls photocatalytic efficiency of CBZ over the hybrid in the degradation process.

In order to further evaluate the degradation mechanism of $\alpha\text{-Fe}_2\text{O}_3/\text{MIL-101}(\text{Cr})$ hybrid, the ESR measurements was carried out to detect the spin reactive $\cdot\text{OH}$ (in aqueous solution) and $\cdot\text{O}_2^-$ (in methanol solution) species by using 5,5-dimethyl-1-pyrroline N-oxide (DMPO) as a spin trapping agent. It can be seen from Fig. 15a, the DMPO- $\cdot\text{OH}$

signals with relative intensities of 1:2:2:1 are clearly observed in the $\alpha\text{-Fe}_2\text{O}_3$ and $\alpha\text{-Fe}_2\text{O}_3/\text{MIL-101}(\text{Cr})$ hybrid, whereas without signal can be detected in the pure MIL-101(Cr) under visible irradiation. Fig. 15b shows the DMPO- $\cdot\text{O}_2^-$ characteristic peaks are detected under visible light irradiation. Compared with pure MIL-101(Cr), the higher intensities of characteristic peaks are also presented in the hybrid. In contrast, no signal is observed for $\alpha\text{-Fe}_2\text{O}_3$. Moreover, the DMPO- $\cdot\text{OH}$ and DMPO- $\cdot\text{O}_2^-$ signals are not existed in the dark condition for all the photocatalysts, indicating that the reactive species are only generated under visible light. These results suggest that the pure MIL-101(Cr) can produce $\cdot\text{O}_2^-$ radicals and the $\alpha\text{-Fe}_2\text{O}_3$ can produce $\cdot\text{OH}$ radicals due to different band edge potential of the photogenerated electrons and holes. The DMPO- $\cdot\text{OH}$ and DMPO- $\cdot\text{O}_2^-$ signals in the $\alpha\text{-Fe}_2\text{O}_3/\text{MIL-101}(\text{Cr})$ hybrid are obviously stronger than those of MIL-101(Cr) and $\alpha\text{-Fe}_2\text{O}_3$ under visible light. These results prove that the hybrid follows the Z-scheme system rather than a traditional heterojunction structure. And, the Z-scheme system shows more effective separating ability of photogenerated electron-hole pairs.

The band edge position of MIL-101(Cr) and $\alpha\text{-Fe}_2\text{O}_3$ were evaluated by Mott-Schottky measurement, as shown in Fig. S9, the flat-band potential (E_{fb}) of the MIL-101(Cr) and $\alpha\text{-Fe}_2\text{O}_3$ was -1.94 and -0.24 V vs. Ag/AgCl, respectively. The potentials were recalculated against RHE according to the equations $E_{RHE} = E_{Ag/AgCl} + 0.059 \times pH + 0.197 \text{ V}$, where the pH was kept constant at pH 7.0. The E_{fb} of the MIL-101(Cr) and $\alpha\text{-Fe}_2\text{O}_3$ was calculated to be -1.33 and 0.37 V vs. RHE, respectively. Here, the MIL-101(Cr) and $\alpha\text{-Fe}_2\text{O}_3$ were analyzed as n-type semiconductors as a result of their positive slopes of epitaxial tangents (see Fig. S9). Some paper verified that the E_{fb} of n-type semiconductor approximately equalled the conduction band (CB) potential [56]. Being estimated with the band gap energy measured by the UV-vis DRS spectrum (see Fig. 9) and the empirical formula $E_{VB} = E_{CB} + E_g$, the valence band (VB) of the MIL-101(Cr) and $\alpha\text{-Fe}_2\text{O}_3$ was calculated as 2.29 and 2.39 V vs. RHE, respectively.

Based on the above experimental results, a possible mechanism is illustrated in Fig. 16. In the prepared hybrid, photoinduced electrons in the CB of $\alpha\text{-Fe}_2\text{O}_3$ firstly transfers and recombines with holes in the VB of MIL-101(Cr). Successively, the migration of charge carrier results in electron accumulating in the CB of MIL-101(Cr) (-1.33 V), and the holes retain in the VB of $\alpha\text{-Fe}_2\text{O}_3$ (2.39 V). Therefore, the accumulated electrons on the CB of MIL-101(Cr) can reduce O_2 to form $\cdot\text{O}_2^-$ radicals due to the CB of MIL-101(Cr) bearing more negative potential than $\text{O}_2/\cdot\text{O}_2^-$ (-0.33 V) [57]. Simultaneously, the holes of $\alpha\text{-Fe}_2\text{O}_3$ provided with much more positive VB potential (2.39 V) than those of $\text{OH}^-/\cdot\text{OH}$ (1.99 V) and $\text{H}_2\text{O}/\cdot\text{OH}$ (2.34 V) can easily oxidize OH^- or H_2O into $\cdot\text{OH}$ radicals [37]. Also, H_2O_2 can generate hydroxyl radicals following by different paths [58] and plays an important role in accelerating the degradation of CBZ. The different paths mainly involve in

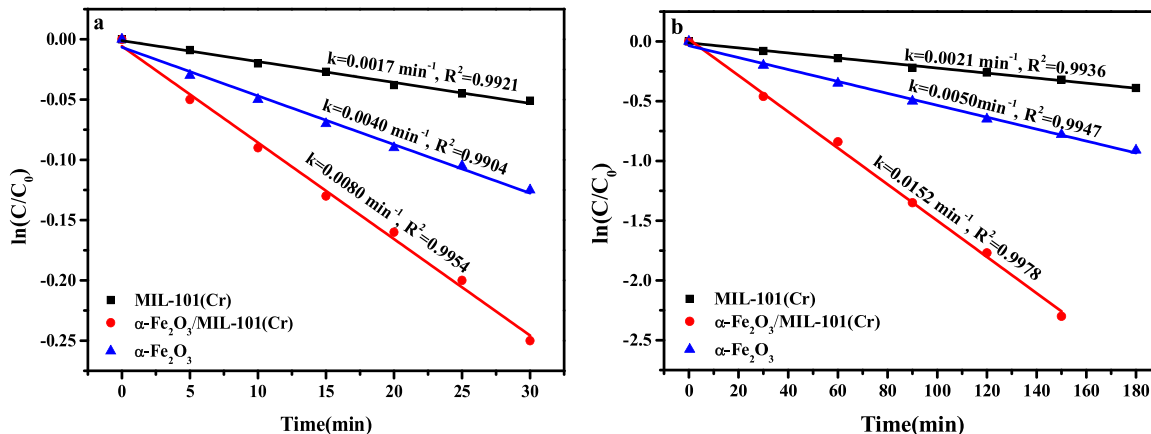


Fig. 11. Linear fit curves for kinetics of CBZ degradation under different conditions: (a) dark and (b) visible light irradiation.

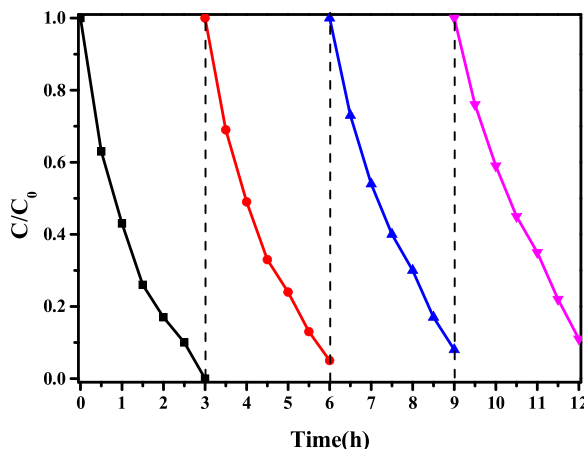


Fig. 12. The cycling runs for the degradation of CBZ over the α -Fe₂O₃(0.3)/MIL-101(Cr).

three processes. First, the H₂O₂ can react with the electron to form ·OH (H₂O₂ + e⁻ → OH⁻ + ·OH); meanwhile, the reaction of H₂O₂ and ·O₂⁻ generate ·OH (H₂O₂ + ·O₂⁻ → OH⁻ + ·OH + O₂); and, the H₂O₂ itself decomposes to produce ·OH under visible light irradiation (H₂O₂ + hν → 2 ·OH). In addition, according to the results of HRTEM and XPS, the hybrid is provided with interface and interfacial interaction between the two phases. Consequently, it can be concluded that the photocatalytic reaction of prepared α-Fe₂O₃(0.3)/MIL-101(Cr) hybrid follows a direct Z-scheme mechanism. With the Z-scheme mechanism, excited electrons from the CB of α-Fe₂O₃ are transferred through the

interface to combine with the photogenerated holes occurred in the VB of MIL-101(Cr), thus retaining the strong reducibility of electron in the CB of MIL-101(Cr) and the strong oxidizability of holes in the VB of α -Fe₂O₃, which not only can accelerate the transferring and separation of photogenerated charges but also can enhance the surface redox ability for efficient degradation of CBZ.

4. Conclusions

In this work, a direct Z-scheme $\alpha\text{-Fe}_2\text{O}_3/\text{MIL-101}(\text{Cr})$ hybrid was prepared by a facile hydrothermal method. The obtained $\alpha\text{-Fe}_2\text{O}_3(0.3)/\text{MIL-101}(\text{Cr})$ hybrid exhibited high photocatalytic performances for CBZ degradation compared to those of MIL-101(Cr) and $\alpha\text{-Fe}_2\text{O}_3$ under the visible light irradiation. The mechanism analysis demonstrated that the electron transferring in the hybrid $\alpha\text{-Fe}_2\text{O}_3/\text{MIL-101}(\text{Cr})$ followed a direct Z-scheme proposed by radical trapping experimental data, ESR measurement, band edge position analysis, HRTEM observation and XPS result. The enhanced photocatalytic activity can be attributed to the formation of the direct Z-scheme and good textural properties of the hybrid. Moreover, the hybrid presented a high efficiency in transforming CBZ into intermediate products and good reusability. Thus, the hybrid $\alpha\text{-Fe}_2\text{O}_3/\text{MIL-101}(\text{Cr})$ provided with excellent performances is a promising visible light response catalyst for the degradation of organic pollutants in wastewater.

Declarations of interest

None.

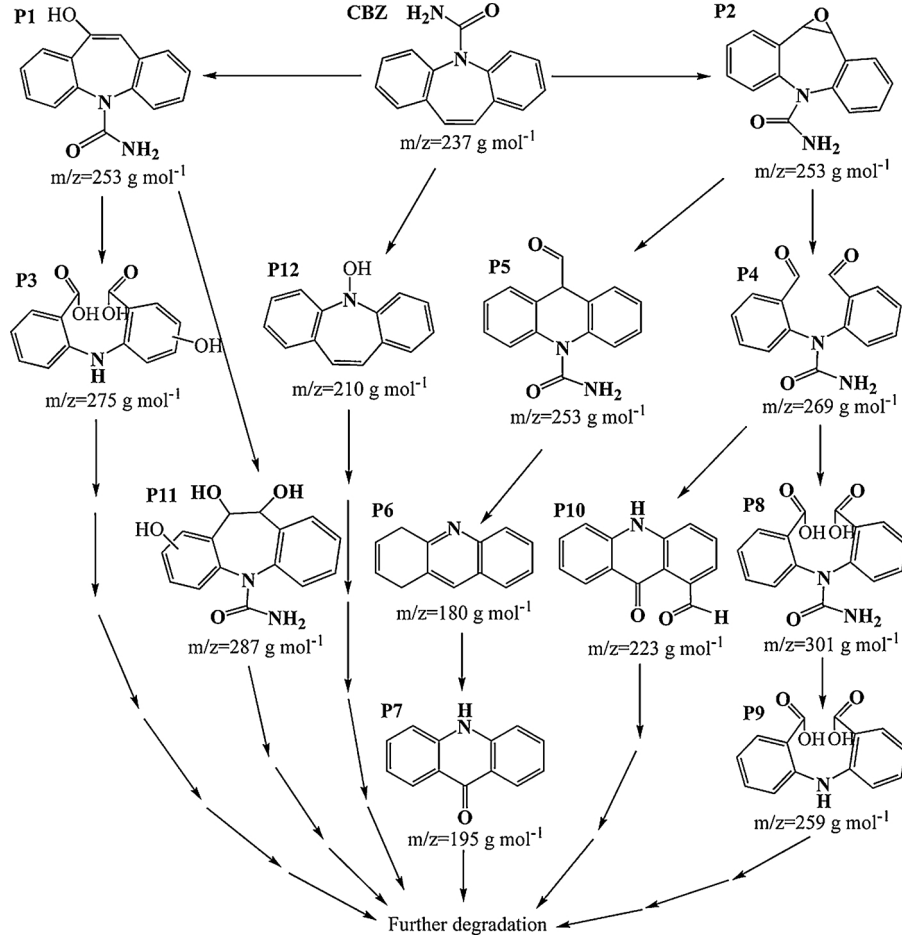


Fig. 13. Possible photodegradation pathways of CBZ over the $\alpha\text{-Fe}_2\text{O}_3(0.3)/\text{MIL-101}(\text{Cr})$.

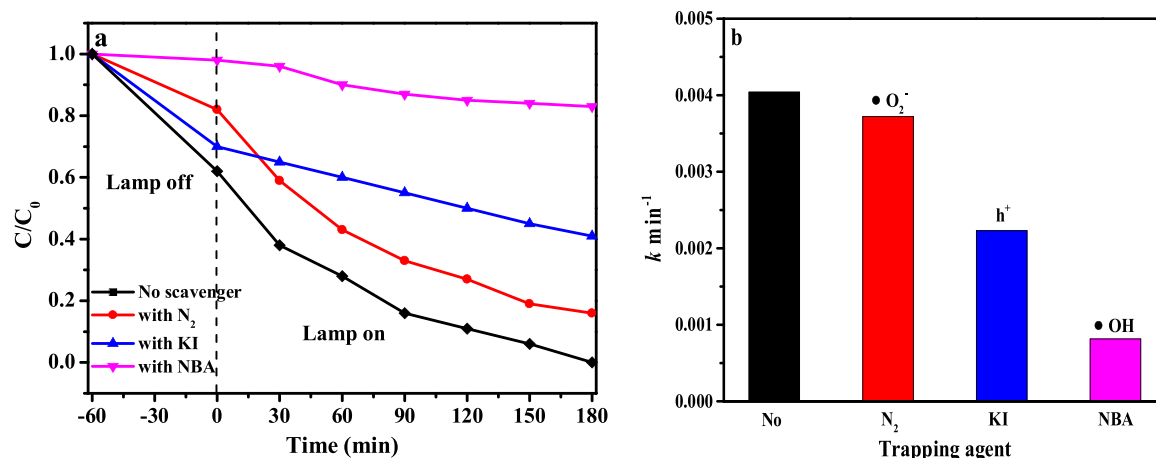


Fig. 14. (a) Effects of radical trapping agents on degradation of CBZ and (b) the corresponding reaction constants.

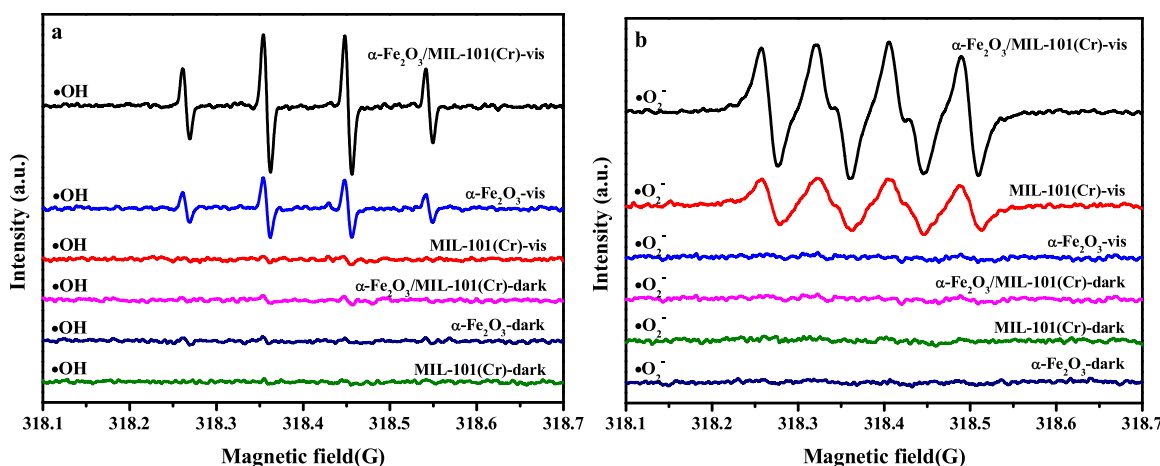


Fig. 15. DMPO spin-trapping ESR spectra recorded for (a) DMPO-·OH in aqueous solution under dark control and visible light irradiation and (b) DMPO-·O₂⁻ in methanol solution under dark control and visible light irradiation.

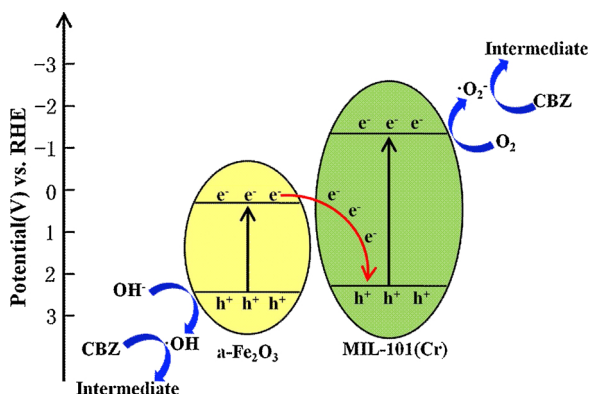


Fig. 16. Proposed photodegradation mechanism of the \$\alpha\text{-Fe}_2\text{O}_3/\text{MIL-101(Cr)}\$ under visible light irradiation.

Acknowledgements

This work was supported by the National Natural Science Foundation of China (nos. 21606193), Hebei Province Funded Project for Introduced Overseas Chinese Scholars (CL201623), and Postdoctoral Research Foundation of Hebei Province (B2016003020).

Appendix A. Supplementary data

Supplementary material related to this article can be found, in the online version, at doi:<https://doi.org/10.1016/j.apcatb.2019.117751>.

References

- [1] H. Yi, M. Jiang, D.L. Huang, G.M. Zeng, C. Lai, L. Qin, C.Y. Zhou, B.S. Li, X.G. Liu, M. Cheng, W.J. Xue, P. Xu, C. Zhang, Advanced photocatalytic Fenton-like process over biomimetic hemin-Bi₂WO₆ with enhanced pH, J. Taiwan Inst. Chem. E 93 (2018) 184–192.
- [2] X.S. Miao, C.D. Metcalfe, Determination of carbamazepine and its metabolites in aqueous samples using liquid chromatography-electrospray tandem mass spectrometry, Anal. Chem. 75 (2003) 3731–3738.
- [3] H.C. Chen, X.N. Wang, W.L. Bi, Y.L. Wu, W.B. Dong, Photodegradation of carbamazepine with BiOCl/Fe₃O₄ catalyst under simulated solar light irradiation, J. Colloid. Interf. Sci. 502 (2017) 89–99.
- [4] W.J. Wang, T.C. An, G.Y. Li, D.H. Xia, H.J. Zhao, J.C. Yu, P.K. Wong, Earth-abundant Ni₂P/g-C₃N₄ lamellar nanohybrids for enhanced photocatalytic hydrogen evolution and bacterial inactivation under visible light irradiation, Appl. Catal. B: Environ. 217 (2017) 570–580.
- [5] H. Yi, M. Yan, D.L. Huang, G.M. Zeng, C. Lai, M.F. Li, X.Q. Huo, L. Qin, S.Y. Liu, X.G. Liu, B.S. Li, H. Wang, M.C. Shen, Y.K. Fu, X.Y. Guo, Synergistic effect of artificial enzyme and 2D nano-structured Bi₂WO₆ for eco-friendly and efficient biomimetic photocatalysis, Appl. Catal. B: Environ. 250 (2019) 52–62.
- [6] J. Zhu, S.H. Wang, J.G. Wang, D.Q. Zhang, H.X. Li, Highly active and durable Bi₂O₃/TiO₂ visible photocatalyst in flower-like spheres with surface-enriched Bi₂O₃ quantum dots, Appl. Catal. B: Environ. 102 (2011) 120–125.
- [7] H. Yi, D.L. Huang, L. Qin, G.M. Zeng, C. Lai, M. Cheng, S.J. Ye, B. Song, X.Y. Ren, X.Y. Guo, Selective prepared carbon nanomaterials for advanced photocatalytic

application in environmental pollutant treatment and hydrogen production, *Appl. Catal. B: Environ.* 239 (2018) 408–424.

[8] Y. Yang, C. Zhang, D.L. Huang, G.M. Zeng, J.H. Huang, C. Lai, C.Y. Zhou, W.J. Wang, H. Guo, W.J. Xue, R. Deng, M. Cheng, W.P. Xiong, Boron nitride quantum dots decorated ultrathin porous g-C₃N₄: intensified exciton dissociation and charge transfer for promoting visible-light-driven molecular oxygen activation, *Appl. Catal. B: Environ.* 245 (2019) 87–99.

[9] W.J. Wang, T.C. An, G.Y. Li, Y.C. Li, J.C. Yu, P.K. Wong, Free-standing red phosphorous/silver sponge monolith as an efficient and easily recyclable macroscale photocatalyst for organic pollutant degradation under visible light irradiation, *J. Colloid. Interf. Sci.* 518 (2018) 130–139.

[10] C.D. Wu, A.G. Hu, L. Zhang, W.B. Lin, A homochiral porous metal-organic framework for highly enantioselective heterogeneous asymmetric catalysis, *J. Am. Chem. Soc.* 127 (2005) 8940–8941.

[11] Y. Qi, Y. Luan, J. Yu, X. Peng, G. Wang, Nanoscaled copper metal-organic framework (MOF) based on carboxylate ligands as an efficient heterogeneously catalyst for aerobic epoxidation of olefins and oxidation of benzylic and allylic alcohols, *Chem. Eur. J.* 21 (2015) 1589–1597.

[12] A. Dhakshinamoorthy, M. Alvaro, H. Garcia, Commercial metal-organic frameworks as heterogeneous catalysts, *Chem. Commun.* 48 (2012) 11275–11288.

[13] L. Pan, M.B. Sander, X.Y. Huang, J. Li, M. Smith, E. Bittner, B. Bockrath, J.K. Johnson, Microporous metal organic materials: promising candidates as sorbents for hydrogen storage, *J. Am. Chem. Soc.* 126 (2004) 1308–1309.

[14] M. Latroche, S. Surblé, C. Serre, C.M. Draznieks, P.L. Llewellyn, J.H. Lee, J.S. Chang, S.H. Jhung, G. Férey, Hydrogen storage in the giant-pore metal-organic frameworks MIL-100 and MIL-101, *Angew. Chem. Int. Ed.* 45 (2006) 8227–8231.

[15] M.C. Wen, G.Y. Li, H.L. Liu, J.Y. Chen, T.C. An, H. Yamashita, Metal-organic framework-based nanomaterials for adsorption and photocatalytic degradation of gaseous pollutants: recent progress and challenges, *Environ. Sci. Nano* 6 (2019) 1006–1025.

[16] C.H. Zhang, L.H. Ai, J. Jiang, Solvothermal synthesis of MIL-53(Fe) hybrid magnetic composites for photoelectrochemical water oxidation and organic pollutant photodegradation under visible light, *J. Mater. Chem. A* 3 (2015) 3074–3081.

[17] H. Wang, X.Z. Yuan, Y. Wu, G.M. Zeng, X.H. Chen, L.J. Leng, H. Li, Synthesis and applications of novel graphitic carbon nitride/metal-organic frameworks mesoporous photocatalyst for dyes removal, *Appl. Catal. B: Environ.* 174–175 (2015) 445–454.

[18] M.T. Wang, D.K. Wang, Z.H. Li, Self-assembly of CPO-27-Mg/TiO₂ nanocomposite with enhanced performance for photocatalytic CO₂ reduction, *Appl. Catal. B: Environ.* 183 (2016) 47–52.

[19] Q. Li, B.D. Guo, J.G. Yu, J.G. Ran, B.H. Zhang, H.J. Yan, J.R. Gong, Highly efficient visible-light-driven photocatalytic hydrogen production of CdS-cluster-decorated graphene nanosheets, *J. Am. Chem. Soc.* 133 (2011) 10878–10884.

[20] C.F. Zhang, L.G. Qiu, F. Ke, Y.J. Zhu, Y.P. Yuan, G.S. Xu, X. Jiang, A novel magnetic recyclable photocatalyst based on metal-organic framework Fe₃O₄@MIL-100(Fe) core-shell for the decolorization of methylene blue dye, *J. Mater. Chem. A* 1 (2013) 14329–14334.

[21] P. Zhou, J. Yu, M. Jaroniec, All-solid-state Z-Scheme photocatalytic systems, *Adv. Mater.* 26 (2014) 4920–4935.

[22] D.H. Xia, W.J. Wang, R. Yin, Z.F. Jiang, T.C. An, G.Y. Li, H.J. Zhao, P.K. Wong, Enhanced photocatalytic inactivation of escherichia coli by a novel Z-scheme g-C₃N₄/m-Bi₂O₃ hybrid photocatalyst under visible light: The role of reactive oxygen species, *Appl. Catal. B: Environ.* 214 (2017) 23–33.

[23] Z.F. Jiang, W.M. Wan, H.M. Li, S.Q. Yuan, H.J. Zhao, P.K. Wong, A hierarchical Z-Scheme α-Fe₂O₃/g-C₃N₄ hybrid for enhanced photocatalytic CO₂ reduction, *Adv. Mater.* 30 (2018) 1706108.

[24] L.C. Xie, Z.H. Yang, W.P. Xiong, Y.Y. Zhou, J. Cao, Y.R. Peng, X. Li, C.Y. Zhou, R. Xu, Y.R. Zhang, Construction of MIL-53(Fe) metal-organic framework modified by silver phosphate nanoparticles as a novel Z-scheme photocatalyst: visible-light photocatalytic performance and mechanism investigation, *Appl. Surf. Sci.* 465 (2019) 103–115.

[25] G. Zhou, M.F. Wu, Q.J. Xing, F. Li, H. Liu, X.B. Luo, J.P. Zou, J.M. Luo, A.Q. Zhang, Synthesis and characterizations of metal-free semiconductor/ MOFs with good stability and high photocatalytic activity for H₂ evolution: a novel Z-scheme heterostructured photocatalyst formed by covalent bonds, *Appl. Catal. B: Environ.* 220 (2018) 607–614.

[26] G. Férey, C. Mellot-Draznieks, C. Serre, F. Millange, J. Dutour, S. Surblé, I. Margiolaki, A chromium terephthalate-based solid with unusually large pore volumes and surface area, *Science* 309 (2005) 2040–2042.

[27] Y.K. Hwang, D.Y. Hong, J.S. Chang, S.H. Jhung, Y.K. Seo, J. Kim, A. Vimont, M. Daturi, C. Serre, G. Férey, Amine grafting on coordinatively unsaturated metal centers of MOFs: consequences for catalysis and metal encapsulation, *Angew. Chem. Int. Ed.* 47 (2008) 4144–4148.

[28] W. Zhen, H. Gao, B. Tian, J. Ma, G. Lu, Fabrication of low adsorption energy Ni-Mo cluster cocatalyst in metal-organic frameworks for visible photocatalytic hydrogen evolution, *ACS Appl. Mater. Interfaces*. 8 (2016) 10808–10819.

[29] S. Patwardhan, G.C. Schatz, Theoretical investigation of charge transfer in metal organic frameworks for electrochemical device applications, *J. Phys. Chem. C* 119 (2015) 24238–24247.

[30] T.H. Zhou, G.Z. Zhang, H.W. Zhang, H. Yang, P.J. Ma, X.T. Li, X.L. Qiu, G. Liu, Highly efficient visible-light-driven photocatalytic degradation of Rhodamine B by a novel Z-scheme Ag₃PO₄/MIL-101/NiFe₂O₄ composite, *Catal. Sci. Technol.* 8 (2018) 2402–2416.

[31] P. Puthiaraj, P. Suresh, K. Pitchumani, Aerobic homocoupling of arylboronic acids catalysed by copper terephthalate metal-organic frameworks, *Green Chem.* 16 (2014) 2865–2875.

[32] M.C. Wen, K. Mori, T. Kamigawa, H. Yamashita, Amine-functionalized MIL-101(Cr) with imbedded platinum nanoparticles as a durable photocatalyst for hydrogen production from water, *Chem. Commun.* 50 (2014) 11645–11648.

[33] R.B. Zhang, B. Du, Q.C. Li, Z.Q. Cao, G. Feng, X.W. Wang, α-Fe₂O₃ nanoclusters confined into UiO-66 for efficient visible-light photodegradation performance, *Appl. Surf. Sci.* 466 (2019) 956–963.

[34] A. Helal, F.A. Harraz, A.A. Ismail, T.M. sami, I.A. Ibrahim, Hydrothermal synthesis of novel heterostructured Fe₂O₃/Bi₂S₃ nanorods with enhanced photocatalytic activity under visible light, *Appl. Catal. B: Environ.* 213 (2017) 18–27.

[35] Y. Wang, C.S. Liu, F.B. Li, C.P. Liu, J.B. Liang, Photodegradation of polycyclic aromatic hydrocarbon pyrene by iron oxide in solid phase, *J. Hazard. Mater.* 162 (2009) 716–723.

[36] S.V. Kalinin, A. Borisevich, D. Fong, Beyond condensed matter physics on the nanoscale: the role of ionic and electrochemical phenomena in the physical functionalities of oxide materials, *ACS Nano* 6 (2012) 10423–10437.

[37] X.J. She, J.J. Wu, H. Xu, J. Zhong, Y. Wang, Y.H. Song, K.Q. Nie, Y. Liu, Y.C. Yang, M.T.F. Rodrigues, R. Vajtai, J. Lou, D.L. Du, H.M. Li, P.M. Ajayan, High efficiency photocatalytic water splitting using 2D α-Fe₂O₃/g-C₃N₄ Z-scheme catalysts, *Adv. Mater.* 7 (2017) 1700025.

[38] S. Jana, A. Mondal, A. Ghosh, Fabrication of stable NiO/Fe₂O₃ heterostructure: a versatile hybrid material for electrochemical sensing of glucose, methanol and enhanced photodecomposition and/photoreduction of water contaminants, *Appl. Catal. B: Environ.* 232 (2018) 26–36.

[39] S.Y. Liu, Y. Zhang, Y. Meng, F. Gao, S.J. Jiao, Y.C. Ke, Fast syntheses of MOFs using nanosized zeolite crystal seeds in situ generated from microsized zeolites, *Cryst. Growth Des.* 13 (2013) 2697–2702.

[40] S.T. Gao, T. Feng, C. Feng, N.Z. Shang, C. Wang, Novel visible-light responsive Ag/AgCl@MIL-101 hybrid materials with synergistic photocatalytic activity, *J. Colloid. Interf. Sci.* 466 (2016) 284–290.

[41] Q.L. Zhu, J. Li, Q. Xu, Immobilizing metal nanoparticles to metal-organic frameworks with size and location control for optimizing catalytic performance, *J. Am. Chem. Soc.* 135 (2013) 10210–10213.

[42] F. Zadehahmadi, S. Tangestaninejad, M. Moghadam, V. Mirkhani, I.M. Baltork, A.R. Khosropour, R. Kardanpour, Synthesis and characterization of manganese(III) porphyrin supported on imidazole-modified chloromethylated MIL-101(Cr): a heterogeneous and reusable catalyst for oxidation of hydrocarbons with sodium peroxide, *J. Solid. State. Chem.* 218 (2014) 56–63.

[43] M. Saikia, D. Bhuyan, L. Saikia, Facile synthesis of Fe₃O₄ nanoparticles on metal organic framework MIL-101(Cr): characterization and catalytic activity, *New J. Chem.* 39 (2015) 64–67.

[44] N. Li, Q.F. Zhu, Y. Yang, J.L. Huang, X.P. Dang, H.X. Chen, A novel dispersive solid-phase extraction method using metal-organic framework MIL-101 as the adsorbent for the analysis of benzophenones in toner, *Talanta* 132 (2015) 713–718.

[45] J.H. Jin, Z.H. Yang, W.P. Xiong, Y.Y. Zhou, R. Xu, Y.R. Zhang, J. Cao, X. Li, C.Y. Zhou, Cu and Co nanoparticles co-doped MIL-101 as a novel adsorbent for efficient removal of tetracycline from aqueous solutions, *Sci. Total Environ.* 650 (2019) 408–418.

[46] H. Khajavi, H.A. Stil, H.P.C.E. Kuipers, J. Gascon, F. Kapteijn, Shape and transition state selective hydrogenations using egg-shell Pt-MIL-101(Cr) catalyst, *ACS Catal.* 3 (2013) 2617–2626.

[47] M.G. Ahmed, T.A. Kandiel, A.Y. Ahmed, I. Kretschmer, F. Rashwan, D. Bahnenmann, Enhanced photoelectrochemical water oxidation on nanostructured hematite photoanodes via p-CaFe₂O₄/n-Fe₂O₃ heterojunction formation, *J. Phys. Chem. C* 119 (2015) 5864–5871.

[48] Q. Liu, F.R. Cao, F.L. Wu, W. Tian, L. Li, Interface reacted ZnFe₂O₄ on a-Fe₂O₃ nanoarrays for largely improved photoelectrochemical activity, *RSC Adv.* 5 (2015) 79440–79446.

[49] D.P. Mohapatra, S.K. Brar, R. Daghbir, R.D. Tyagi, P. Picard, R.Y. Surampalli, P. Drogui, Photocatalytic degradation of carbamazepine in wastewater by using a new class of whey-stabilized nanocrystalline TiO₂ and ZnO, *Sci. Total Environ.* 485 (2014) 263–269.

[50] X.Y. Gao, X.C. Zhang, Y.W. Wang, S.Q. Peng, B. Yue, C.M. Fan, Photocatalytic degradation of carbamazepine using hierarchical BiOCl microspheres: some key operating parameters, degradation intermediates and reaction pathway, *Chem. Eng. J.* 273 (2015) 156–165.

[51] M. Nawaz, W. Miran, J. Jang, D.S. Lee, One-step hydrothermal synthesis of porous 3D reduced graphene oxide/TiO₂ aerogel for carbamazepine photodegradation in aqueous solution, *Appl. Catal. B: Environ.* 203 (2017) 85–95.

[52] J.X. Lu, L. Li, C.S. Guo, Y. Zhang, W. Meng, Photocatalytic degradation of carbamazepine by tailored BiPO₄: efficiency, intermediates and pathway, *Appl. Catal. B: Environ.* 130–131 (2013) 285–292.

[53] L.L. Bo, K.B. He, N. Tan, B. Gao, Q.Q. Feng, J.D. Liu, L. Wang, Photocatalytic oxidation of trace carbamazepine in aqueous solution by visible-light-driven ZnIn₂S₄: performance and mechanism, *J. Environ. Manage.* 190 (2017) 259–265.

[54] S.P. Sun, X. Zeng, A.T. Lemley, Kinetics and mechanism of carbamazepine degradation by a modified Fenton-like reaction with ferric-nitritotriacetate complexes, *J. Hazard. Mater.* 252–253 (2013) 155–165.

[55] E. Kaiser, C. Prasse, M. Wagner, K. Broder, T.A. Ternes, Transformation of oxcarbazepine and human metabolites of carbamazepine and oxcarbazepine in wastewater treatment and sand filters, *Environ. Sci. Technol.* 48 (2014) 10208–10216.

[56] M.T. Qamar, M. Aslam, Z.A. Rehan, M.T. Soomiro, J.M. Basahi, I.M.I. Ismail, T. Almeelbi, A. Hameed, The influence of p-type Mn₃O₄ nanostructures on the photocatalytic activity of ZnO for the removal of bromo and chlorophenol in natural sunlight exposure, *Appl. Catal. B: Environ.* 201 (2017) 105–118.

[57] L.B. Jiang, X.Z. Yuan, G.M. Zeng, J. Liang, X.H. Chen, H.B. Yu, H. Wang, Z.B. Wu, J. Zhang, T. Xiong, In-situ synthesis of direct solid-state dual Z-scheme WO₃/g-C₃N₄/Bi₂O₃ photocatalyst for the degradation of refractory pollutant, *Appl. Catal. B: Environ.* 227 (2018) 376–385.

[58] X.Y. Li, Y.H. Pi, Q.B. Xia, Z. Li, J. Xiao, TiO₂ encapsulated in Salicylaldehyde-NH₂-MIL-101(Cr) for enhanced visible light-driven photodegradation of MB, *Appl. Catal. B: Environ.* 191 (2016) 192–201.